



Deformation and residual stress of T-shaped joints fabricated by laser-arc hybrid welding for steel bridge members

Gang Chen¹ · Mikihiro Hirohata¹ · Kengo Hyoma² · Naoyuki Matsumoto² · Koutarou Inose²

Received: 1 August 2023 / Accepted: 28 November 2023 / Published online: 21 December 2023
© The Author(s) 2023

Abstract

A series of experiments and analyses were performed for applying laser-arc hybrid welding to fabricating steel bridge components. Two-pass fully penetrated T-shaped joints using high-performance steel (SBHS400) having a 15-mm thickness were produced using hybrid welding. T-shaped joints having identical dimensions were manufactured using conventional arc welding. Without considering the inter-pass cooling time, the duration of hybrid welding was reduced by roughly 83% in comparison to that for GMAW. The average out-of-plane deformation caused by hybrid welding was decreased by 67% compared to arc welding. The fully coupled thermal elastic–plastic analyses were performed to replicate the distribution of residual stress in as-welded T-shaped joints. The analytical results indicated that the tensile residual stress range in hybrid-welded T-shaped joints was approximately one third (1/3) of that in arc-welded T-shaped joints. The weld joints produced by hybrid welding may have advantages over those produced by arc welding in terms of reducing welding deformation, decreasing welding residual stresses, and shortening welding time when manufacturing large steel bridge components.

Keywords Laser-arc hybrid welding · T-shaped joints · Deformation and residual stress · Thermal elastic–plastic analysis · Steel bridge components

1 Introduction

Laser welding, a well-known welding process, is capable of producing weldments with faster travel speed, deep penetration, high precision, and reduced welding distortion compared to arc welding [1]. Due to these merits, laser welding is extensively utilized in many industries, including the automotive industry, aerospace industry, and shipping industry. However, due to the intricate heat and fluid interaction, laser-welded joints may encounter several weld defects, including porosity, spatters, root sag, humping, and underfilling [2–4].

As an attractive alternative approach to mitigate or even solve the problems, laser-arc hybrid welding (also known as hybrid

welding) has gained growing industrial attention on account of the synergic effects between laser welding and arc welding [5]. The synergetic effects facilitate achieving high welding speed, deep penetration, and low welding deformation. Furthermore, broadening gap bridgeability and gap tolerances are achieved. The laser beam provides intense energy density into narrow areas, enabling deep penetration, increased welding speed, and reduced welding distortion compared with arc welding. Meanwhile, the filler materials introduced during arc welding enable improved gap bridgeability and gap tolerances compared to laser welding [6]. In our previous investigation, when 15-mm-thick steel plates were joined by laser-arc hybrid welding, one-pass full-penetration welding could be achieved. However, for fabricating same dimensional specimens, six passes were required by conventional arc welding. In addition, the duration of hybrid welding was decreased by 98%, and the angular distortion for weld joints produced by hybrid welding was 95% lower than that for weld joints produced by arc welding [7]. Additionally, hybrid welding could achieve sound welds with up to 2-mm misalignment via adjusting the welding travel speed and the position of the hybrid head [8]. For structural steels having a thickness of 15 mm, hybrid welding could bridge maximum gap widths of 0.8 mm [9]. When laser welding was conducted

Recommended for publication by Commission XV - Design, Analysis, and Fabrication of Welded Structures

✉ Mikihiro Hirohata
hirohata@civil.eng.osaka-u.ac.jp

¹ Graduate School of Engineering, Osaka University, Osaka, Japan

² IHI Corporation, Tokyo, Japan

with cold wire feeding, it was possible to bridge a gap of up to 0.6 mm, whereas, without filler material, the maximum value of gap width achievable was 0.2 mm. The laser/GMA hybrid welding showed its ability to bridge gaps as wide as 1.0 mm in 2.1-mm-thick sheets [10]. Thanks to these merits, hybrid welding was extensively used in various industries [11–14].

High-performance steel (HPS) features excellent strength, weldability, and toughness, making it possible to reduce costs and upgrade productivity for constructing steel bridges compared to conventional steel grades. In an investigation, the hybrid design, which combined HPS and traditional steel grades, could obtain considerable and definite savings for both steel weight and total costs [15]. In recent years, Japan has developed a novel steel grade, SBHS (Steels for Bridge High-Performance Structure). It is fabricated by thermo-mechanical controlled processing (TMCP). Compared to conventional welded structural steels, SBHS features high strength and toughness, and excellent weldability and workability. SBHS was specified by JIS G3140 in 2008. Employing SBHS in fabricating steel bridge components is projected to result in reducing bridge construction expenses and increasing the robustness of steel structures. As a result, it was identified as the material for this investigation.

In prior studies, hybrid welding has been widely applied in joining steel bridge components and extensively studied from various perspectives, encompassing investigations into residual stress, distortion, mechanical properties related to toughness, and susceptibility to cold cracking [7, 16–21]. This research aims to further broaden the scope of hybrid welding applications in joining steel structures and validate the effectiveness of hybrid welding in manufacturing steel structures. T-shaped specimens, regarded as general and widely used joints in steel bridge members, were fabricated using hybrid and arc welding. A series of experiments were conducted on the as-welded T-joints to measure residual stress and welding deformation. Moreover, numerical simulations were performed via fully coupled thermal elastic–plastic analyses to obtain the detailed distribution of residual stress and welding deformation. The comparison between experimental and numerical simulation results confirmed the validity of hybrid welding in terms of welding time, distortion, and residual stress. This provides a theoretical foundation for the application of laser-arc hybrid welding in the fabrication of steel bridge components.

2 Experimental procedures

2.1 T-shaped specimen

Figure 1 demonstrates the geometric dimensions of a T-shaped specimen, which consists of two 15-mm-thick steel plates. The geometric shape of the bottom plate and

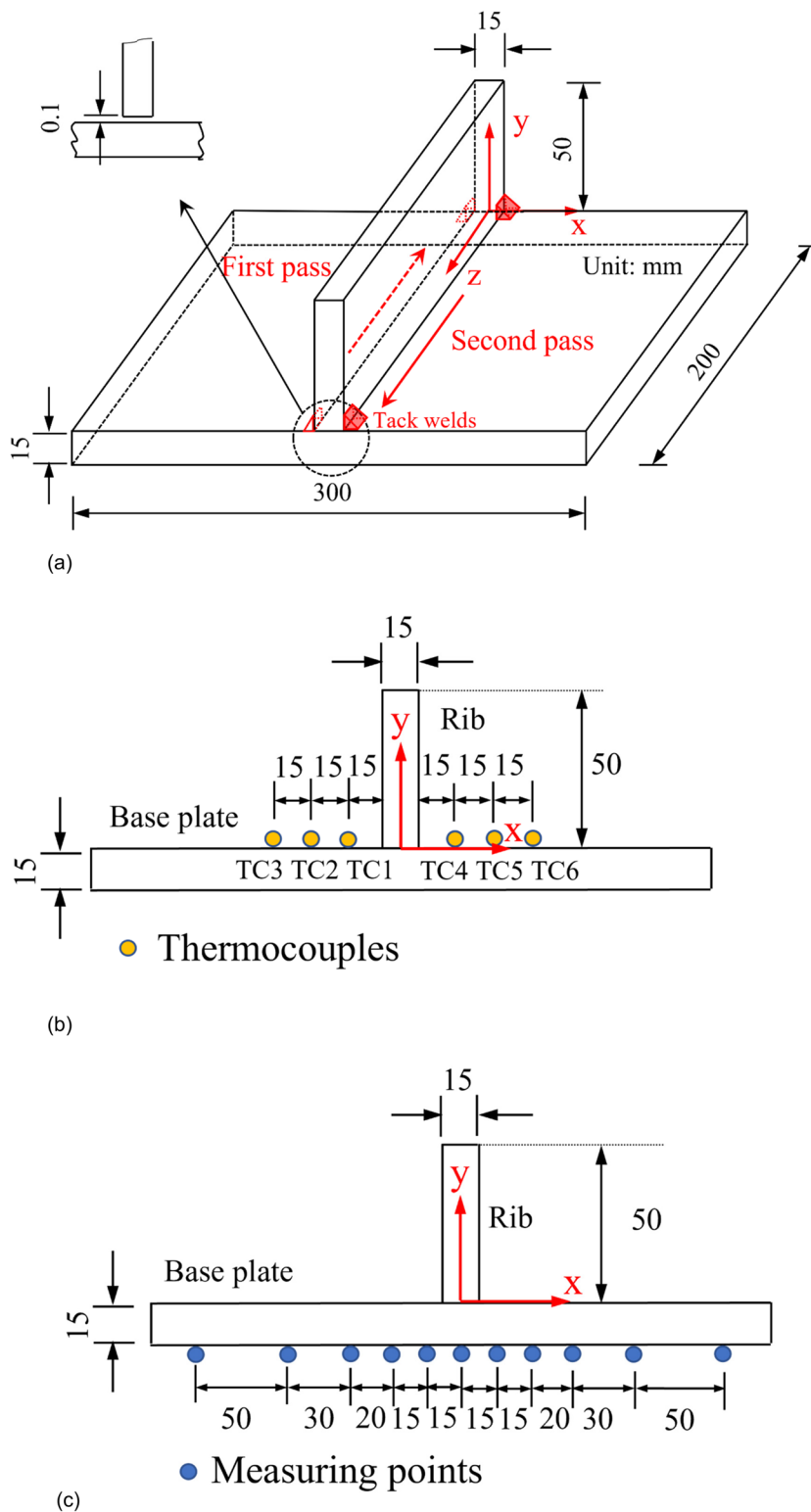
rib plate was rectangular. The geometric dimensions of the bottom plate were 300 mm in length and 200 mm in width. At the midspan of the bottom plate, a 50-mm-high rib plate was welded in two single passes by hybrid and arc welding. Four specimens were fabricated, two using hybrid welding and the other two using arc welding. They were named LA400-1,2 and A400-1,2. In this investigation, the steel plates were made of SBHS400. The filler material used was YGW11 as specified in JIS Z 3312, with a 1.2-mm wire diameter. Table 1 lists the chemical compositions and measured mechanical properties (as per mill sheet values provided by the mill maker) of SBHS400 and the welding wire. The base metal has a nominal yield strength above 400 MPa and a nominal tensile strength ranging from 490 to 640 MPa. The filler material possesses a nominal yield strength of 490 MPa and a nominal tensile strength of 590 MPa. Before being joined by fillet welding, tack welding was performed for obtaining the right alignment between the bottom plate and rib plate. Tack welding was employed to attach the rib plate to the bottom plate at both ends of the weld lines. While tack welding was carried out, there was still a small gap, later confirmed in the macroscopic photographs of T-shaped joints using arc welding, between the bottom plate and the rib plate. The thermocouples were attached at six positions ($x = \pm 22.5, \pm 37.5, \pm 52.5$ mm; $y = 0$ mm; $z = 100$ mm) as illustrated in Fig. 1. They were employed to capture and monitor the temperature throughout the entire welding process.

2.2 Welding procedures

The hybrid welding process combines fiber laser welding and MIG arc welding simultaneously. The YLR-20000 laser oscillator from IPG Photonics Corporation is a fiber laser, providing a maximum power output of 20 kW. This apparatus possesses a focal length of 250 mm, a beam diameter of 0.6 mm, and a defocusing distance of -5 mm. The power supply utilized for GMAW was a DP350 digital pulse welding power source manufactured by DAIHEN Corporation. The shielding gas utilized was a mixture of Ar and 5% CO₂, delivered at 20 ℓ/min. The experimental setup is shown in Fig. 2. The leading heat source was set to be the laser beam. The spacing separating the laser beam and electric arc was adjusted to be 1 mm. The arc torch was inclined at a 45-degree angle, while the laser beam was inclined at a 75-degree angle from the vertical. Table 2 illustrates the welding parameters for both hybrid and arc welding.

Hybrid welding and GMAW were used to create double-pass fillet welds on both sides of the rib plate. No mechanical restraint was applied throughout the entire welding process. After the inter-pass temperature had cooled below 50 °C for hybrid welding and 100 °C for arc welding, the second pass was performed.

Fig. 1 T-shaped specimen



2.3 Measuring out-of-plane deformation and residual stress

To investigate the characteristics of distortion and residual stress of two-pass T-shaped joints by hybrid and arc welding,

several measurements were carried out.

The out-of-plane deformation was measured at the seven points ($x=0, \pm 50, \pm 100, \pm 150$ mm; $y = -15$ mm; $z = 100$ mm) for hybrid- and arc-welded T-shaped joints. Residual stresses (in the welding and cross directions) were

Table 1 Chemical compositions and mechanical properties of SBHS400 and filler material

Material	Chemical compositions (mass%)								Yield strength (MPa)	Tensile strength (MPa)	Elongation (%)
	C	Si	Mn	P	S	Ni	Cr	Fe			
SBHS400	0.11	0.29	1.36	0.009	0.001	0.01	0.02	bal	503	567	22
YGW11	0.04	0.73	1.66	0.015	0.009	—	—	bal	422	515	30

obtained through the X-ray diffraction technique (XRD) at the specified measuring points ($x=0, \pm 15, \pm 30, \pm 50, \pm 80, \pm 130$ mm; $y=-14.7$ mm; $z=120$ mm). Prior to measuring the residual stress, the area surrounding the measurement points underwent electropolishing to a depth of about 0.3 mm beneath the surface to eliminate the effect of surface treatment.

Figure 3 demonstrates the cross-sectional macroscopic images of both types of weld joints obtained after measuring out-of-plane deformation and residual stress. Two-pass fully penetrated T-shaped joints were achieved by hybrid welding, thanks to its deep penetration. However, arc welding failed to achieve full penetration.

3 Fully coupled thermal elastic–plastic analysis

3.1 Numerical analysis for hybrid welding

To explore thoroughly the distributions of distortion and residual stress, the fully coupled temperature-displacement analysis was performed by Abaqus ver. 6.18 for simulating the aforementioned hybrid welding experiment. As demonstrated in Fig. 4, the analysis model was created based on the specimen, LA400-1. The element type used was an 8-node thermally coupled brick with trilinear displacement and temperature. This analysis was implemented by applying heat input to the fusion zone. Therefore, concerning the mesh division, we referenced the fusion zone of the cross-sectional macroscopic image shown in Fig. 3, roughly plotting the shape of the fusion zone. The element size along the welding seam direction was set as 2 mm. An element birth technique was employed to replicate metal deposition accompanied by the movement of heat sources during the welding process. Figure 4 illustrates the assumed mechanical boundary conditions. As for the thermal boundary condition, the heat transfer was established by considering the heat exchange from the analytical model surfaces to the ambient atmosphere. In the experimental procedure, a gap existed between two steel plates, and they were fixed by tack welds. The numerical model took into consideration the influence of tack welds and the initial gap, with a gap width assumed to be 0.1 mm. Additionally, for the model, the ambient temperature and the initial condition temperature were both set to the atmospheric

temperature. Concerning the material properties, as shown in Fig. 5, this paper referenced previous research [22–24].

Hybrid welding features rapid heating and cooling, leading to the hardening of heat-affected zone (HAZ), as well as weld metal (WM). Consequently, the Vickers hardness of hybrid-welded T-shaped joints was measured based on prior studies [18, 25]. Figure 6 demonstrates the measuring points and the Vickers hardness of T-shaped joints fabricated by hybrid welding. The weld metal exhibited a hardness approximately 1.5 times higher than that of the base metal (BM). Similarly, the maximum value of Vickers hardness of the HAZ was roughly twice that of the BM. In this investigation, the WM of average Vickers hardness was divided by the average Vickers hardness of the BM to determine mechanical characteristics of WM. The average Vickers hardness represented the sum of Vickers hardness measurements at various measurement points within the corresponding regions (WM, HAZ, and BM) divided by the total number of measurement points. According to the test results, the filler material exhibited the yield strength and tensile strength that were 1.5 times greater than the BM in the numerical simulation. The average Vickers hardness of HAZ was not considered. As shown in Fig. 6 (b) and (c), the Vickers hardness in WM and BM exhibited small fluctuation amplitudes with corresponding small standard deviations, rendering the average Vickers hardness in WM and BM representative. However, in the case of HAZ, there was a significant fluctuation amplitude and a large standard deviation. Therefore, the average Vickers hardness in HAZ could not be employed.

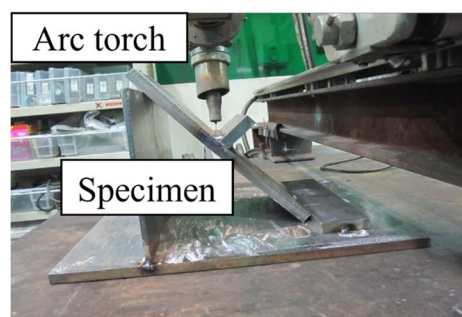
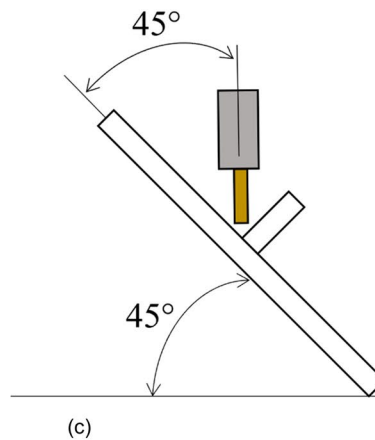
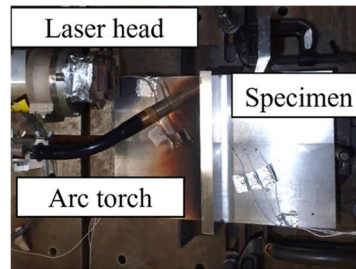
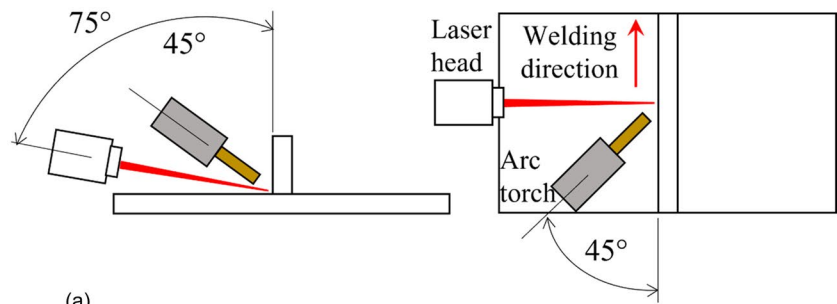
In accordance with the previous investigation [18], the load in the numerical model was simulated as a uniform body heat flux originating from both the laser and arc. As shown in Fig. 4, the red region represented the laser heat input; the purple region represented the arc heat input. However, this model neglected the spacing separating the laser and arc heat sources.

The magnitudes of the laser (Q_L) and arc (Q_A) heat input were determined by Eqs. (1) and (2), respectively.

$$Q_L = \frac{P \cdot \eta_L}{v} \quad (\text{J/mm}) \quad (1)$$

$$Q_A = \frac{I \cdot V \cdot \eta_A}{v} \quad (\text{J/mm}) \quad (2)$$

Here, P is the laser energy (kW), I is the arc welding current (A), V is the arc welding voltage (V), v is the

Fig. 2 Experimental setup

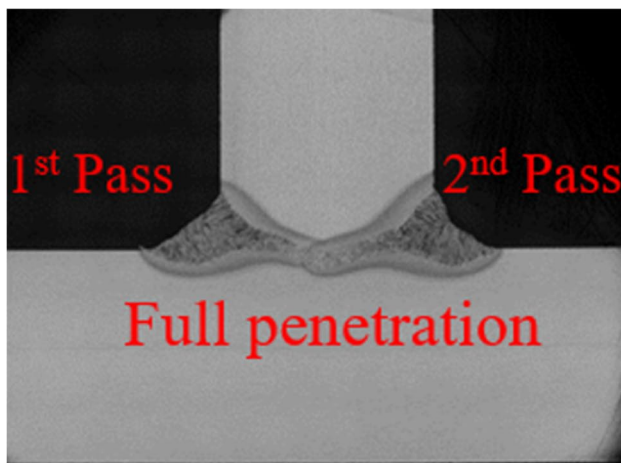
welding travel speed (mm/s), η_L is the laser welding efficiency, and η_A is the arc welding efficiency.

The laser and arc welding efficiency varies depending on the welding process. Nevertheless, the laser and arc welding efficiencies typically range from 0.5 to 0.9 [26, 27] and 0.6 to

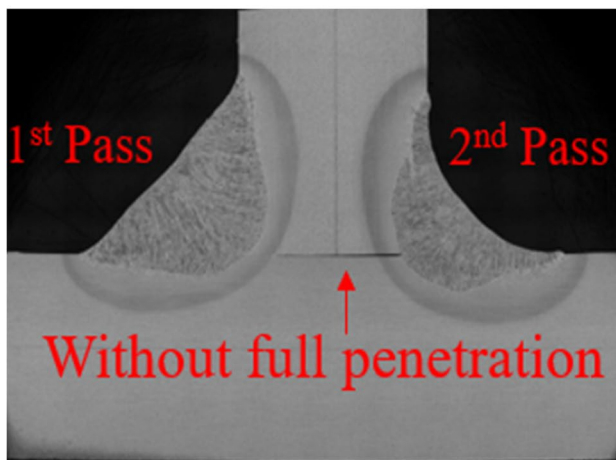
0.8 [28]. To achieve good agreement between the temperature history obtained from the experiment and the simulation, the laser and arc welding efficiency was adjusted. Eventually, for both welding passes, the thermal efficiencies were determined as 0.7 for the laser (η_L) and 0.8 for the arc (η_A).

Table 2 Welding conditions

Welding condition	Welding pass	Laser power (kW)	Welding speed (m/min)	Arc current (A)	Arc voltage (V)	Heat input (J/mm)		
						Laser	Arc	Total
LA400-1	1	6.9	1.0	156	27.1	414	254	668
	2	6.9	1.0	155	27.3	414	254	668
LA400-2	1	7.0	1.0	166	28.1	420	280	700
	2	7.0	1.0	178	24.0	420	256	676
A400-1	1		0.174	275	36.5		3461	3461
	2		0.174	275	35.5		3366	3366
A400-2	1		0.174	287	35.2		3484	3484
	2		0.174	288	35.2		3496	3496



(a)



(b)

Fig. 3 Cross-sectional macroscopic photographs of hybrid-welded and arc-welded T-shaped joints

3.2 Numerical analysis for arc welding

Figure 7 demonstrates the numerical model and mesh division, created based on specimen, A400-1. The element type used

was an 8-node thermally coupled brick with trilinear displacement and temperature. The longitudinal element length was set to 20 mm. As for other analytical conditions, they were the same as those conditions demonstrated in Section 3.1. The arc welding efficiency was adjusted until the experimental temperature history matched well with the numerical temperature history. Eventually, the value of arc welding efficiency (η_A) was decided to be 0.8 for both welding passes.

The Vickers hardness of arc-welded T-shaped joints was also measured. Figure 8 demonstrates the measuring points and the Vickers hardness of arc-welded T-shaped joints. The Vickers hardness of WM, HAZ, and BM was almost the same. The similarity in Vickers hardness among the WM, HAZ, and BM could be attributed to the relatively small temperature gradient induced by arc welding compared to hybrid welding. The reduced temperature gradient fostered a more uniform grain recrystallization process, resulting in the development of finer crystalline structures instead of a coarse metallographic structure. This homogeneity led to the similarity in hardness among these regions. As a result, the arc welding simulation in this study did not introduce the average Vickers hardness ratio.

4 Results and discussions

4.1 Temperature history

Figure 9 illustrates the experimental and analytical temperature histories of the hybrid-welded T-joint. It was validated that the analytical temperature histories matched well with the experimental histories, except for the temperature histories obtained from the two thermocouples (TC1 and TC 4) near the fusion zone. This discrepancy was linked to the generation of spatters during the hybrid welding experiments, which flew onto the thermocouples, causing a sharp increase in temperature. Moreover, the as-welded hybrid-welded T-shaped joints showed spatters near the thermocouples (TC1 and TC 4), which in turn confirmed the assumption.

Fig. 4 FE model for hybrid welding

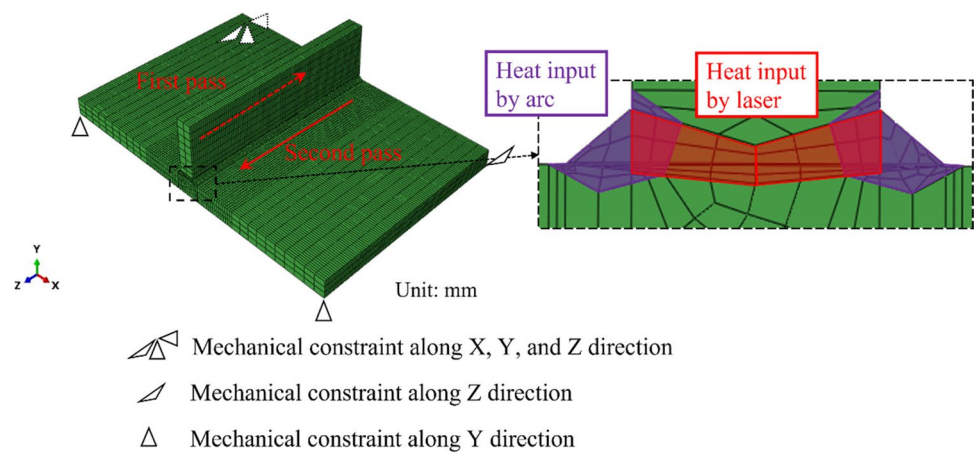


Figure 10 illustrates the temperature histories of the arc-welded T-joint obtained from the analysis and the experiment. Apart from the thermocouples (TC1 and TC4), the experimental and analytical temperature histories exhibited acceptable agreement. This discrepancy was considered to be for the same reason as observed in hybrid welding.

4.2 Welding deformation

Figure 11 shows the out-of-plane deformation ($z = 100$ mm) derived from the analysis and experiment. For hybrid welding, the analytical results could reproduce the experimental results. As for arc welding, although the analytical results were slightly larger than the experimental results, they still remained within an acceptable range.

When comparing the out-of-plane deformation derived from the two types of welding experiments, the average out-of-plane deformation was 0.86 mm for hybrid-welded T-shaped joints and 2.73 mm for arc-welded T-shaped joints, respectively. The average out-of-plane deformation for hybrid welding was decreased by 67% compared to that for arc welding. In addition, the total heat input in hybrid welding was significantly lower compared to that in arc welding, as illustrated in Table 2. As a result, the out-of-plane deformation of hybrid-welded T-shaped joints was suppressed in comparison to the arc-welded T-shaped joints. Furthermore, it indicated that hybrid welding, due to the reduction of out-of-plane deformation, may be advantageous from the perspectives of time and economic costs when fabricating the steel structural members.

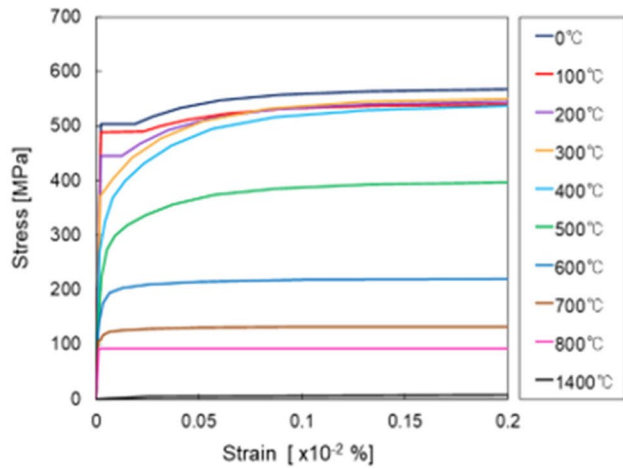
4.3 Residual stress

Figure 12 (a) and (b) illustrate the distribution of residual stresses in both types of T-shaped joints along the cross

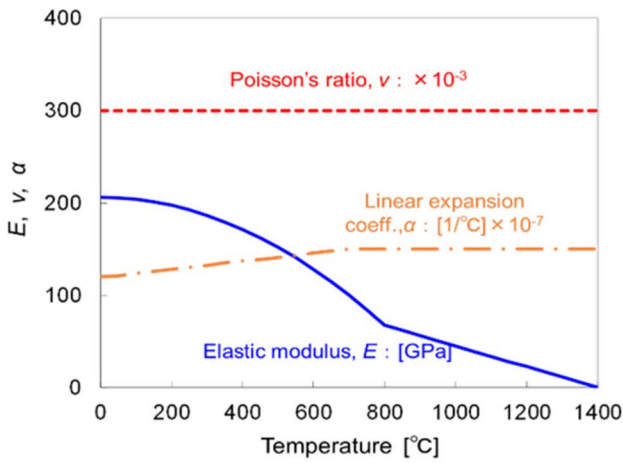
and welding directions obtained by the experiments. The maximum value of transverse tensile residual stress, a significant factor that could reduce fatigue life, was generated in the T-shaped weld joints produced by hybrid welding. The maximum value of compressive residual stress along the welding seam direction, a significant factor that could weaken the compressive load-carrying capacity, occurred in the arc-welded T-shaped joints.

Figure 13 (a) and (b) demonstrate the experimental and analytical residual stress in both types of T-shaped joints. Regarding the hybrid welding simulation, the analytical results generally replicated the experimental results in both directions, indicating that the proposed hybrid welding simulation model was reasonable. Concerning the arc welding simulation, the analytical results could generally reproduce the trend of experimental results, yet the analytical values ($x = 0$ mm) deviated dramatically from the experimental values. Several main reasons could explain this phenomenon as follows: firstly, the positions of electrochemical grinding may have a small deviation, and even minor deviations could cause significant variation in residual stress because the residual stress at $x = 0$ mm exhibited drastic changes. Secondly, there was a time interval between electrochemical grinding and residual stress measurement, and the metal surface after electrochemical grinding developed imperceptible rust and corrosion, resulting in deviations in the measurement. Thirdly, at this point ($x = 0$ mm), the measurement error for X-ray diffraction (XRD) escalated [29]. In summary, comparing the experimental results to the analytical ones, the proposed arc welding simulation model was generally reasonable despite the observed deviations.

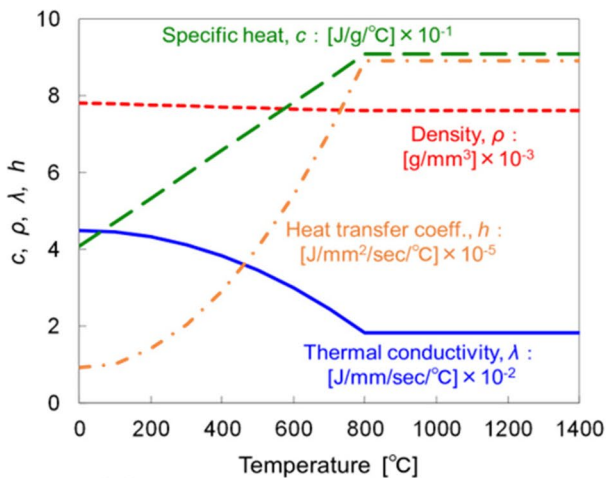
As demonstrated in Fig. 13(a), by comparing the residual stress distributions derived from the experiments and simulations, the experimental maximum value of transverse tensile residual stress was generated in specimen LA400-1. However, the analytical maximum tensile residual stress in both types of weld joints was 365 MPa and 413 MPa,



(a)

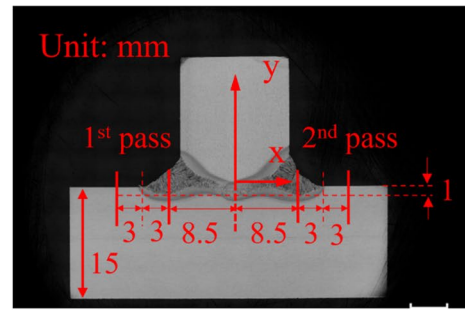


(b)

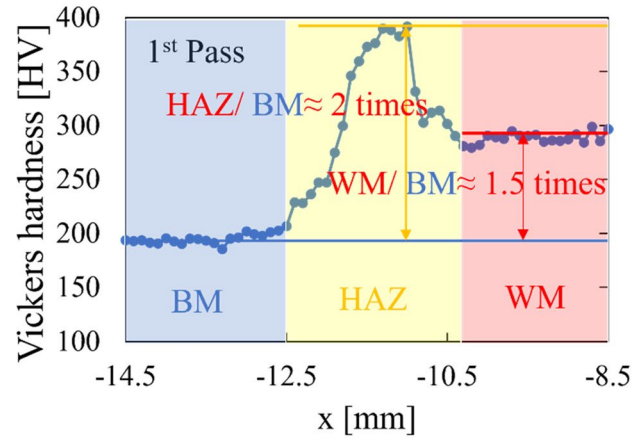


(c)

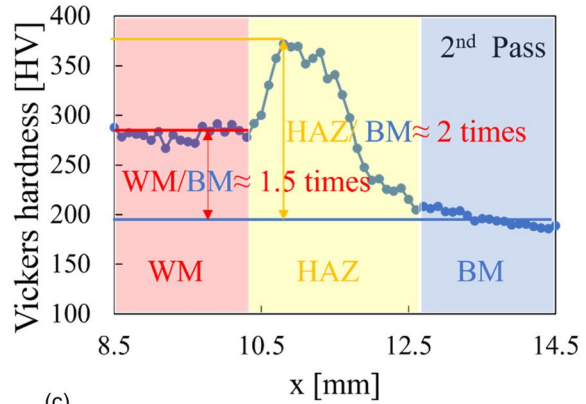
Fig. 5 Mechanical properties and physical constants used for simulation



(a)



(b)



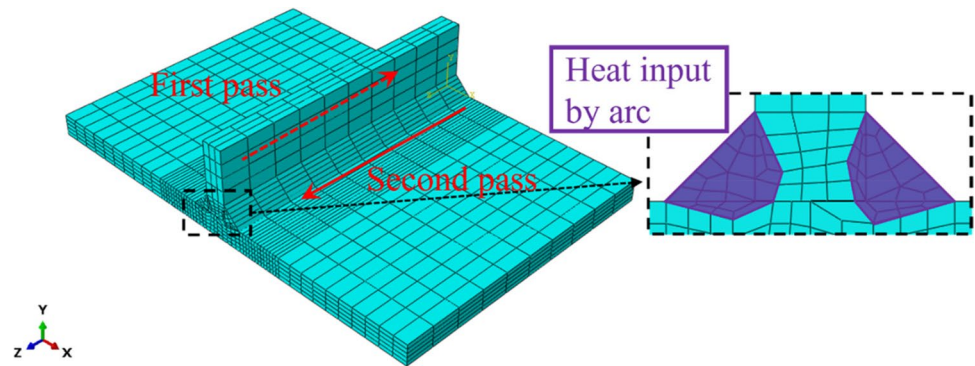
(c)

Fig. 6 The test results of hybrid-welded T-joint

respectively. The analytical maximum residual stress of the hybrid-welded joint was 48 MPa less than that of the arc-welded joint, indicating that the hybrid-welded joints may outperform arc-welded joints in terms of fatigue life. Moreover, combined with the maximum tensile residual stress (128 MPa) in specimen LA400-2, the viewpoint was strengthened.

As demonstrated in Fig. 13(b), by comparing the longitudinal residual stress distributions, the experimental maximum compressive residual stress in specimen LA400-1 was -125 MPa compared to the value

Fig. 7 FE model for arc welding



(-286 MPa) in specimen A400-1. The analytical maximum tensile residual stress in both types of weld joints was 43 MPa and 353 MPa, respectively. The analytical maximum compressive residual stress in both types of weld joints was -62 MPa and -331 MPa, respectively. In addition, the tensile residual stress values in the hybrid-welded joints ranged from roughly -8 to 7 mm. In contrast, the tensile residual stress values in the arc-welded joints ranged from roughly -20 to 25 mm. Hence, the tensile residual stress zone in hybrid-welded joints was roughly one-third of arc-welded joints. Beyond this range, the compressive residual stress was generated along the welding direction to counteract the tensile residual stress and weaken the load-carrying capacity of T-shaped joints. The range and values of tensile residual stress in the hybrid-welded T-shaped joints were dramatically decreased compared to the arc-welded T-shaped joints. Meanwhile, the maximum compressive stress was also significantly reduced. Taking into consideration the small welding deformation induced by hybrid welding, the compressive load-carrying capacity of hybrid-welded T-shaped joints may outperform that of arc-welded T-shaped joints. Furthermore, as illustrated in Fig. 12(b), the experimental maximum compressive residual stress of specimen LA400-2 was 66 MPa less than that of specimen A400-2. The viewpoint was reinforced that the compressive load-carrying capacity of hybrid-welded T-shaped joints may outperform that of arc-welded T-shaped joints.

5 Conclusions

The effectiveness of hybrid welding in manufacturing T-shaped joints having 15 mm-thick steel plates using SBHS400 by two-pass full penetration was investigated through experiments and analyses. The following conclusions are the primary outcomes acquired.

- (1) Within the scope of the experiments, hybrid welding was able to achieve two-pass fully penetrated T-shaped joints due to its deep penetration capabilities. However, the arc-welded T-shaped joints failed to achieve two-pass full-penetration. Without considering inter-pass cooling time, the welding time for hybrid welding was 83% shorter than arc welding.
- (2) On account of the reduced heat input, the average out-of-plane deformation in weld joints produced by hybrid welding was decreased by 67% in comparison to those fabricated by arc welding.
- (3) Fully coupled thermal elastic–plastic analyses were performed to reproduce the fabrication processes, and the effectiveness of the proposed hybrid and arc welding simulation models was verified. According to the analytical results, the maximum transverse residual stress generated in the hybrid-welded T-joint was decreased by 48 MPa. Based on the experimental results, the maximum average compressive residual stress generated in the hybrid-welded T-shaped joints in the welding direction was reduced by about 132 MPa.

Fig. 8 The Vickers hardness test results of arc-welded T-joint

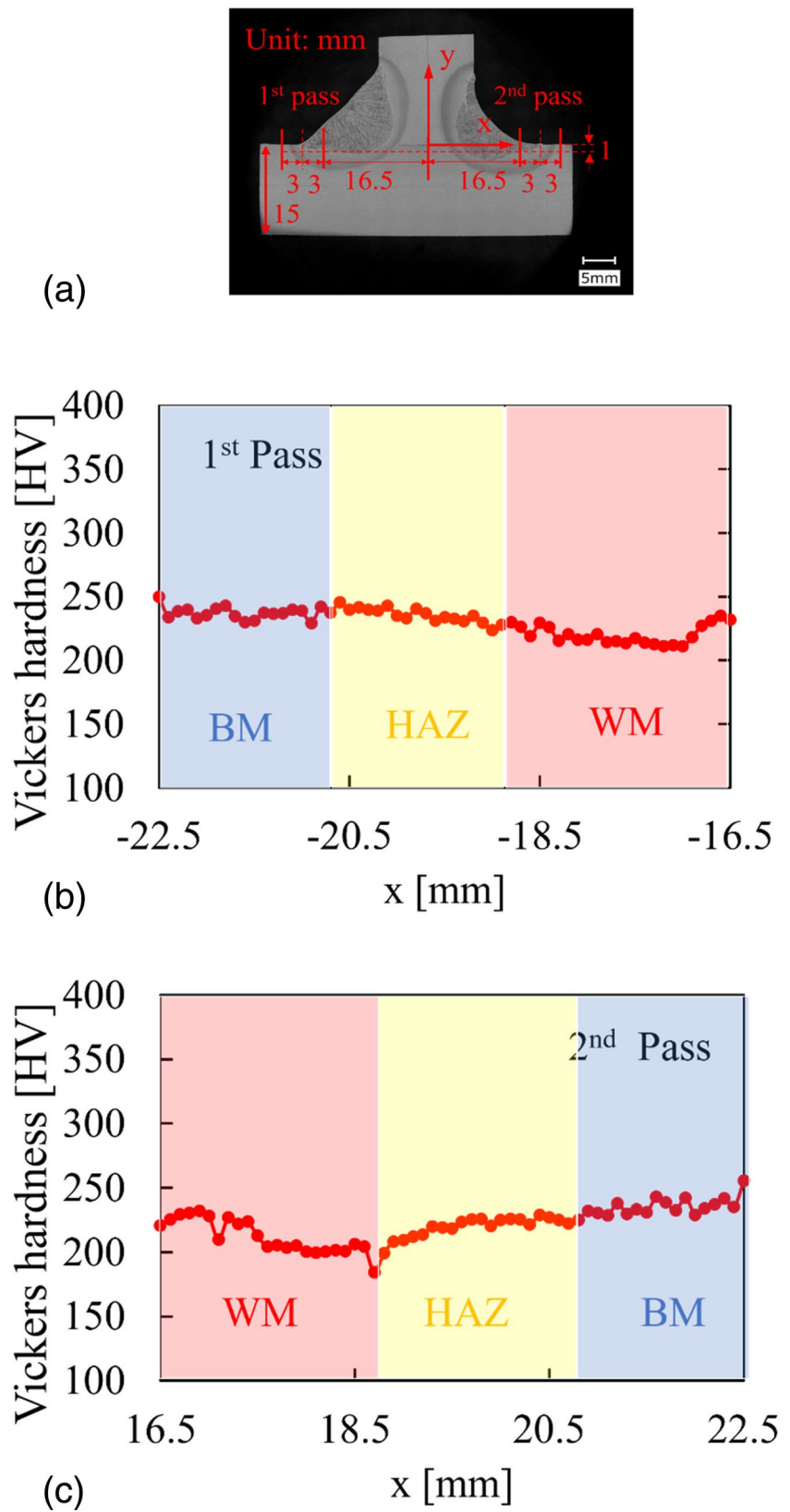


Fig. 9 The experimental and analytical temperature histories of the hybrid-welded T-joint

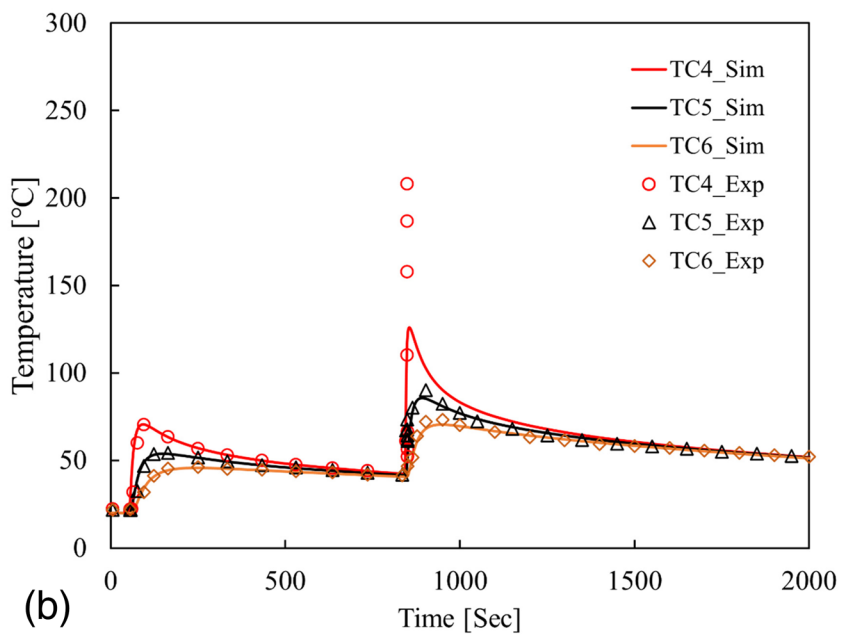
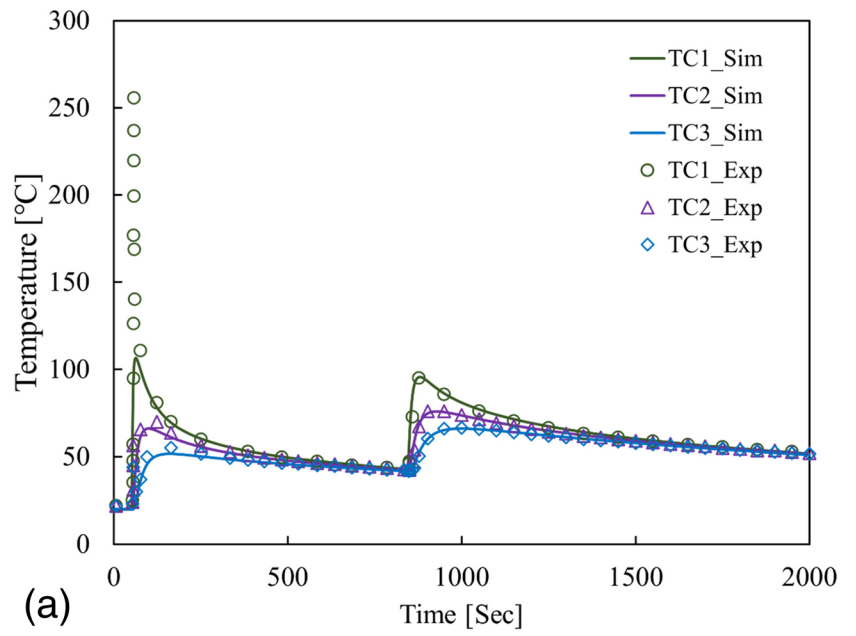
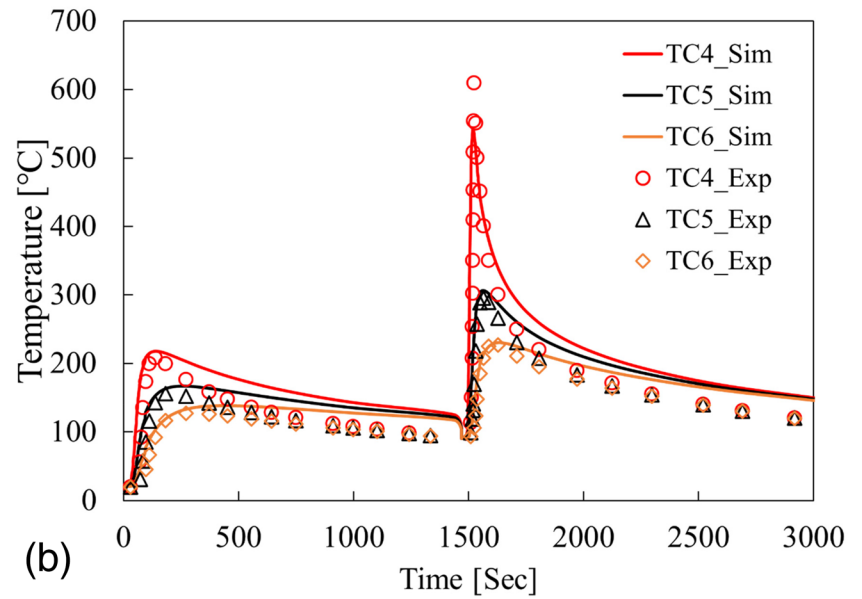
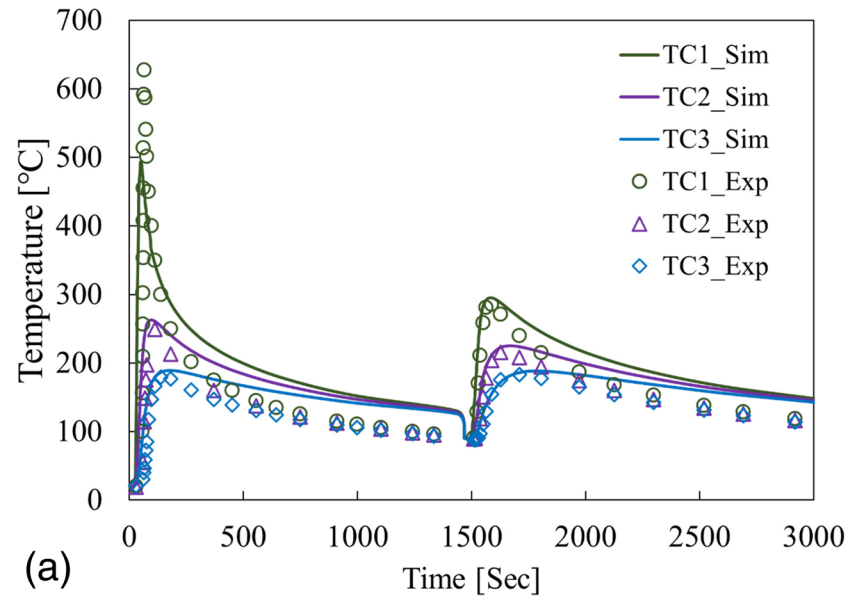


Fig. 10 The temperature histories of the arc-welded T-joint obtained by the analysis and experiment



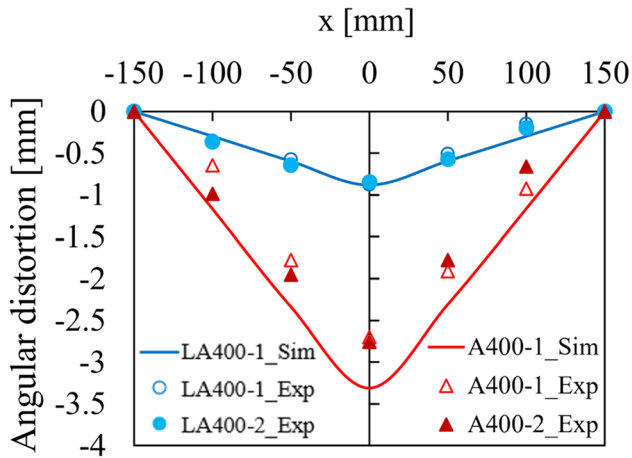
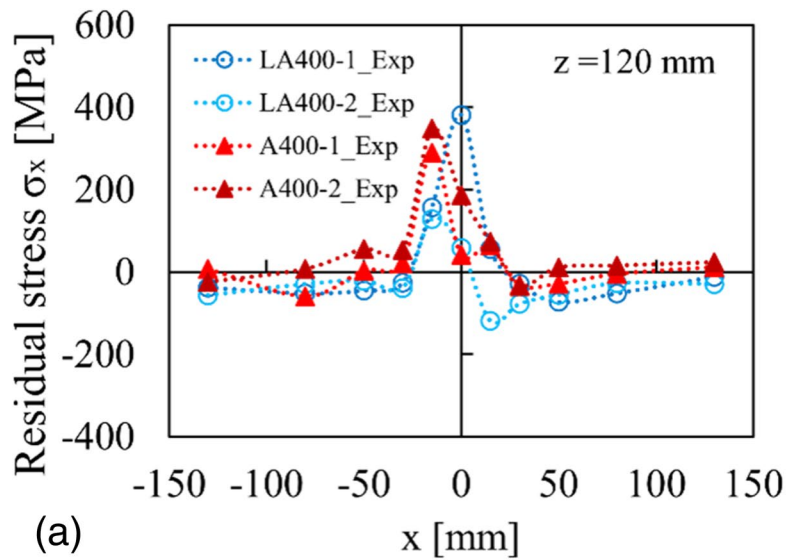
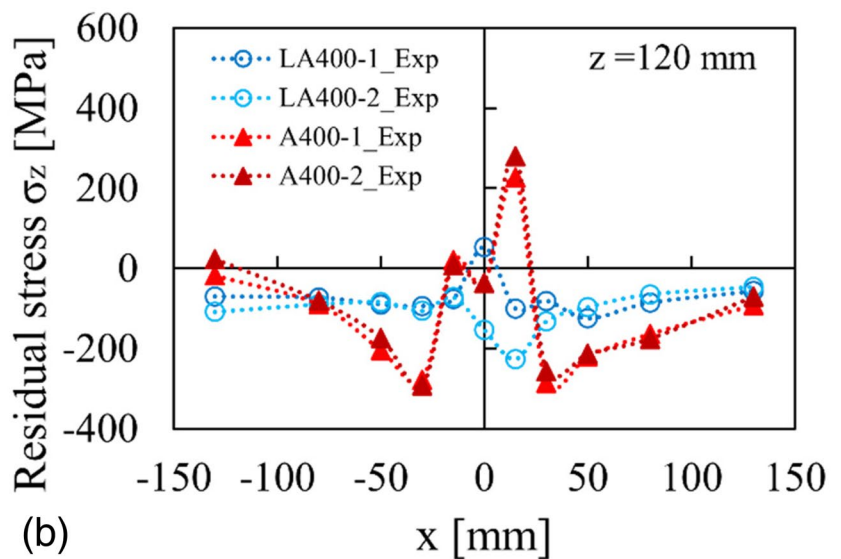


Fig. 11 Out-of-plane deformation distortions by hybrid and arc welding

Fig. 12 Residual stress obtained from the experiments

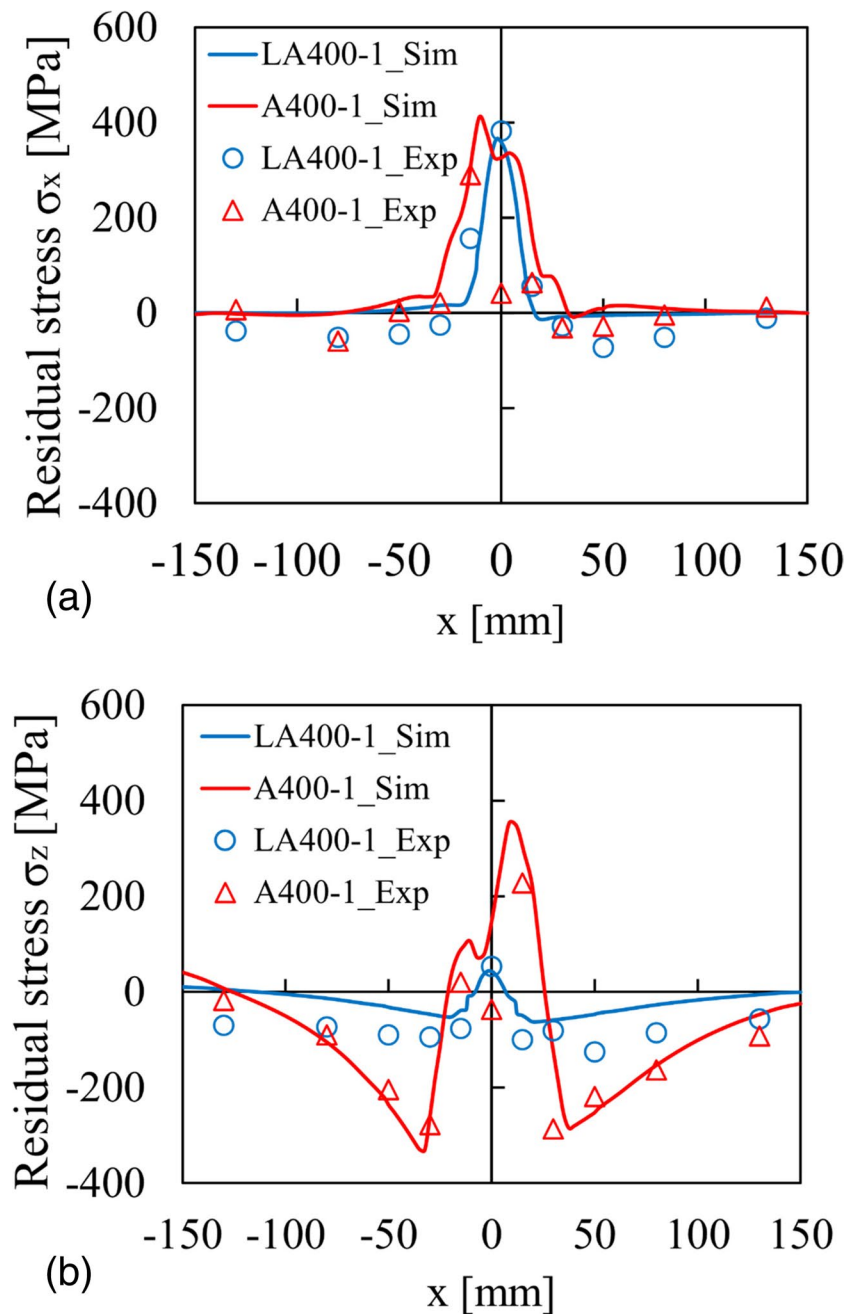


(a)



(b)

Fig. 13 Residual stresses by the experiments and simulations for hybrid and arc welding



Funding Open access funding provided by Osaka University. Partial financial support for this investigation was provided by a grant from the Japan Iron and Steel Federation (JISF) for steel structure research and education during the fiscal years 2019 and 2020. Also, the research was supported by JST SPRING, Grant Number JPMJSP2138.

Data Availability Data sharing is not applicable to this article.

Declarations

Conflict of interest The authors declare no competing interests.

Open Access This article is licensed under a Creative Commons Attribution 4.0 International License, which permits use, sharing, adaptation, distribution and reproduction in any medium or format, as long as you give appropriate credit to the original author(s) and the source, provide a link to the Creative Commons licence, and indicate if changes were made. The images or other third party material in this article are included in the article's Creative Commons licence, unless indicated otherwise in a credit line to the material. If material is not included in the article's Creative Commons licence and your intended use is not permitted by statutory regulation or exceeds the permitted use, you will

need to obtain permission directly from the copyright holder. To view a copy of this licence, visit <http://creativecommons.org/licenses/by/4.0/>.

References

- Moore PL, Howse DS, Wallach ER (2004) Microstructures and properties of laser/arc hybrid welds and autogenous laser welds in pipeline steels. *Sci Technol Weld Join* 9:314–322. <https://doi.org/10.1179/136217104225021652>
- Jiang M, Chen X, Chen YB, Tao W (2020) Mitigation of porosity defects in fiber laser welding under low vacuum. *J Mater Process Technol* 276:116385. <https://doi.org/10.1016/j.jmatp.2019.116385>
- Fujii H, Umakoshi H, Aoki Y, Nogi K (2004) Bubble formation in aluminium alloy during electron beam welding. *J Mater Process Technol* 155:1252–1255. <https://doi.org/10.1016/j.jmatp.2004.04.141>
- Kutsuna M, Yan C (1998) Study on porosity formation in laser welds in aluminium alloys (Report 1): effects of hydrogen and alloying elements. *Weld Int* 12:937–949. <https://doi.org/10.1080/0950711980944>
- Ascari A, Fortunato A, Orazi L, Campana G (2012) The influence of process parameters on porosity formation in hybrid LASER-GMA welding of AA6082 aluminum alloy. *Opt Laser Technol* 44:1485. <https://doi.org/10.1016/j.optlastec.2011.12.014>
- Üstündağ Ö, Fritzsche A, Avilov V et al (2018) Study of gap and misalignment tolerances at hybrid laser arc welding of thick-walled steel with electromagnetic weld pool support system. *Procedia CIRP* 74:757–760. <https://doi.org/10.1016/j.procir.2018.08.016>
- Hirohata M, Chen G, Morioka K, Hyoma K, Matsumoto N, Inose K (2021) An investigation on laser-arc hybrid welding of one-pass full-penetration butt joints for steel bridge members. *Weld World* 66:515–527. <https://doi.org/10.1007/s40194-021-01221-0>
- Rethmeier M, Gook S, Lammers M, Gumenyuk A (2009) Laser-hybrid welding of thick plates up to 32 mm using a 20 kW fibre laser. *J Jpn Weld Soc* 27:74–77
- Kristensen JK (2009) Thick plate CO₂-laser based hybrid welding of steels. *Weld World* 53:47–57
- Aalderink BJ, Pathiraj B, Aarts RGKM (2010) Seam gap bridging of laser based processes for the welding of aluminium sheets for industrial applications. *Int J Adv Manuf Technol* 48:143–154
- Reutzel EW, Sullivan MJ, Mikesic DA (2006) Joining pipe with the hybrid laser-GMAW process: weld test results and cost analysis. *Weld J* 85:66–71
- Olschok S, Reisinger U, Dilthey U (2007) Robot application for laser-GMA hybrid welding in shipbuilding. In: Proc. of the Laser Materials Processing Conference ICALEO 2007, Orlando, USA, pp 308–315. <https://doi.org/10.2351/1.5061084>
- Walz C, Springer IS, El Rayes M, Seefeld T, Sepold G (2001) Hybrid welding of steel for offshore applications. In: ISOPE International Ocean and Polar Engineering Conference, p. ISOPE-I-01-380
- Stauffer H (2006) Laser hybrid welding and laser brazing at audi and VW. *Weld World* 50:44–50. <https://doi.org/10.1007/BF03266535>
- Barker MG, Schrage SD (2000) High-performance steel bridge design and cost comparisons. *Transp Res Rec* 1740(1):33–39. <https://doi.org/10.3141/1740-05>
- Derakhshan E, Yazdian N, Craft B, Smith S, Kovacevic R (2018) Numerical simulation and experimental validation of residual stress and welding distortion induced by laser-based welding processes of thin structural steel plates in butt joint configuration. *Opt Laser Technol* 104:170–1828
- Ma N, Li L, Huang H, Chang S, Murakawa H (2015) Residual stresses in laser-arc hybrid welded butt-joint with different energy ratios. *J Mater Process Technol* 220:36–45
- Hirohata M, Takeda F, Suzuki M, Inose K, Matsumoto N, Abe D (2019) Influence of laser-arc hybrid welding conditions on cold cracking generation. *Weld World* 63:1407–1416
- Inose K, Owaki K, Kanbayashi J, Nakanishi Y (2012) Functional assessment of laser arc hybrid welded joints and their application for bridge construction. *Weld World* 56:118–124
- Inose K, Kanbayashi J, Abe D, Matsumoto N, Nakanishi Y (2013) Design and welding method for high strength steel structure using laser-arc hybrid welding. *Weld World* 57:657–664
- Inose K, Yamaoka H, Nakanishi Y, Minami F (2017) Toughness assessments of laser arc-hybrid welds of ultra high strength steel. *Weld World* 61:955–961
- Furumura F, Abe T, Okabe T, Kim W-J (1986) A uniaxial stress strain formula of structural steel at high temperature and its application to thermal deformation analysis of steel frames. *J Struct Constr Eng (Trans AIJ)* 363:110–117 in Japanese
- Nakagawa H, Suzuki H (1999) Ultimate temperatures of steel beams subjected to fire. *Steel Constr Eng* 6(22):57–65 in Japanese
- Kim Y-C, Lee J-Y, Inose K (2007) Dominant factors for high accurate prediction of distortion and residual stress generated by fillet welding. *Steel Struct* 7:93–100
- Zhang P, Li SX, Zhang ZF (2011) General relationship between strength and hardness. *Mater Sci Eng A* 529:62–73. <https://doi.org/10.1016/j.msea.2011.08.061>
- Yasuda K, Kitani Y (2000) Metallurgical characteristics of CO₂ laser weld metal in heavy plates. *Weld Int* 14(10):787–793. <https://doi.org/10.1080/09507110009549269>
- Miyazaki Y, Katayama S (2016) Power attenuation and focus shift of solid state laser beam caused by laser-induced plume. *Weld Int* 30(11):846–857. <https://doi.org/10.1080/09507116.2016.1142207.24>
- Joseph A, Harwig D, Farson DF, Richardson R (2003) Measurement and calculation of arc power and heat transfer efficiency in pulsed gas metal arc welding. *Sci Technol Weld Join* 8(6):400–406. <https://doi.org/10.1179/136217103225005642>
- Prevey PS (1986) X-ray diffraction residual stress techniques, ASM Handbook. ASM 10:380–392

Publisher's Note Springer Nature remains neutral with regard to jurisdictional claims in published maps and institutional affiliations.